Identification of the Late Devonian back-arc magmatism in the Chinese Eastern Tianshan

Long Du [a,b,*], Xiaoping Long [b], Chao Yuan [c], Yunying Zhang [d], Zongying Huang [c], Hongli Zhu [e]

[a] *Research Center of Continental Dynamics, College of Earth Science and Engineering, Shandong University of Science and Technology, Qingdao 266590, China*
[b] *State Key Laboratory of Continental Dynamics, Department of Geology, Northwest University, Xi'an 710069, China*
[c] *State Key Laboratory of Isotope Geochemistry, Guangzhou Institute of Geochemistry, Chinese Academy of Sciences, Guangzhou 510640, China*
[d] *Key Laboratory of Ocean and Marginal Sea Geology, South China Sea Institute of Oceanology, Innovation Academy of South China Sea Ecology and Environmental Engineering, Chinese Academy of Sciences, Guangzhou 510301, China*
[e] *Center of Deep Sea Research, Institute of Oceanography, Chinese Academy of Sciences, Qingdao 266071, China*

ARTICLE INFO

ABSTRACT

Identifcation of subduction to back-arc tectonic transitions is critical to the study of accretionary orogens. Some new geochronological and geochemical data for the Late Devonian (380–361 Ma) Kezier mafic–felsic complex and Tuwu granitic pluton in this study have well recorded such transition feature in the Chinese Eastern Tianshan orogen. The Kezier gabbro is classified as high-Al basalt given their high Al contents ($Al_2O_3 > 17$ wt%). They were originated from a depleted mantle fluxed by fertile mantle components at shallow depths under hydrous condition. Both the Kezier and Tuwu granites show geochemical characteristics of high total alkali, Ga/Al, HFSE, low CaO, and strongly negative Ba, Sr, and Eu anomalies, demonstrating a close affinity with A-type granites. The granites were probably generated by high temperature melting (zircon saturation temperature up to 916 °C) of crustal rocks under a low-pressure (<0.8–1.0 GPa) condition. These rocks can help identify the Late Devonian back-arc extensional event in the Eastern Tianshan. This extensional event contemporaneous with the onset of the earliest arc magmatic records southward rejuvenating. The back-arc extensional with crustal high-temperature melting event can be reconciled with the Kangguer Ocean rollback, which forced the arc rifting occur on the Dananhu fore-arc side during the Late Devonian.

1. Introduction

Accretionary orogens develop at convergent plate margins due to the ongoing subduction of oceanic lithosphere and commonly comprise arcs, back-arc basins, accretionary prisms, ophiolitic mélanges, and possibly continental fragments (e.g., Cawood et al., 2009). Generally, tectonic transition from arc to back-arc basin, accompanied by crustal thinning, arc tearing, and development of arc–back-arc system, has played a distinctive role in the assembly of accretionary orogens (Collins, 2002; Magni, 2019). The records of the inception formation of back-arc basins are hence crucial for understanding the evolution and geodynamic properties of accretionary orogenies (Collins, 2002; Magni, 2019; Sdrolias and Müller, 2006). However, in ancient orogenic belts, the evidences of *syn*-extensional deformation and sedimentation may be obscured by later geological events, which makes it difficult to recognize

such transitions (e.g., Harris, 2004; Zhang et al., 2020). In these cases, magmatism generated in such processes can provide crucial clues in regard to identifying the arc–back-arc transitions (Grevemeyer et al., 2021; Zhang et al., 2018). It is generally envisioned that magmatism at the back-arc are controlled by pressure-release partial melting of a heterogeneous mantle (e.g., Grevemeyer et al., 2021), which may differ from the arc-type in terms of composition with certain intraplate features, such as oceanic-island basalt (OIB), A-type granitoids, and bimodal rock associations (Ferrari, 2004; Magni, 2019; Shinjo and Kato, 2000). Therefore, investigating the changes in geochemical characteristics of magmatic rocks (e.g., from arc- to intraplate-like magmatism) could provide vital clues for a tectonic transition from arc to back-arc basin.

As a representative accretionary orogen, the Central Asian orogenic belt (CAOB) was indeed formed by interrupted opening, evolution, and
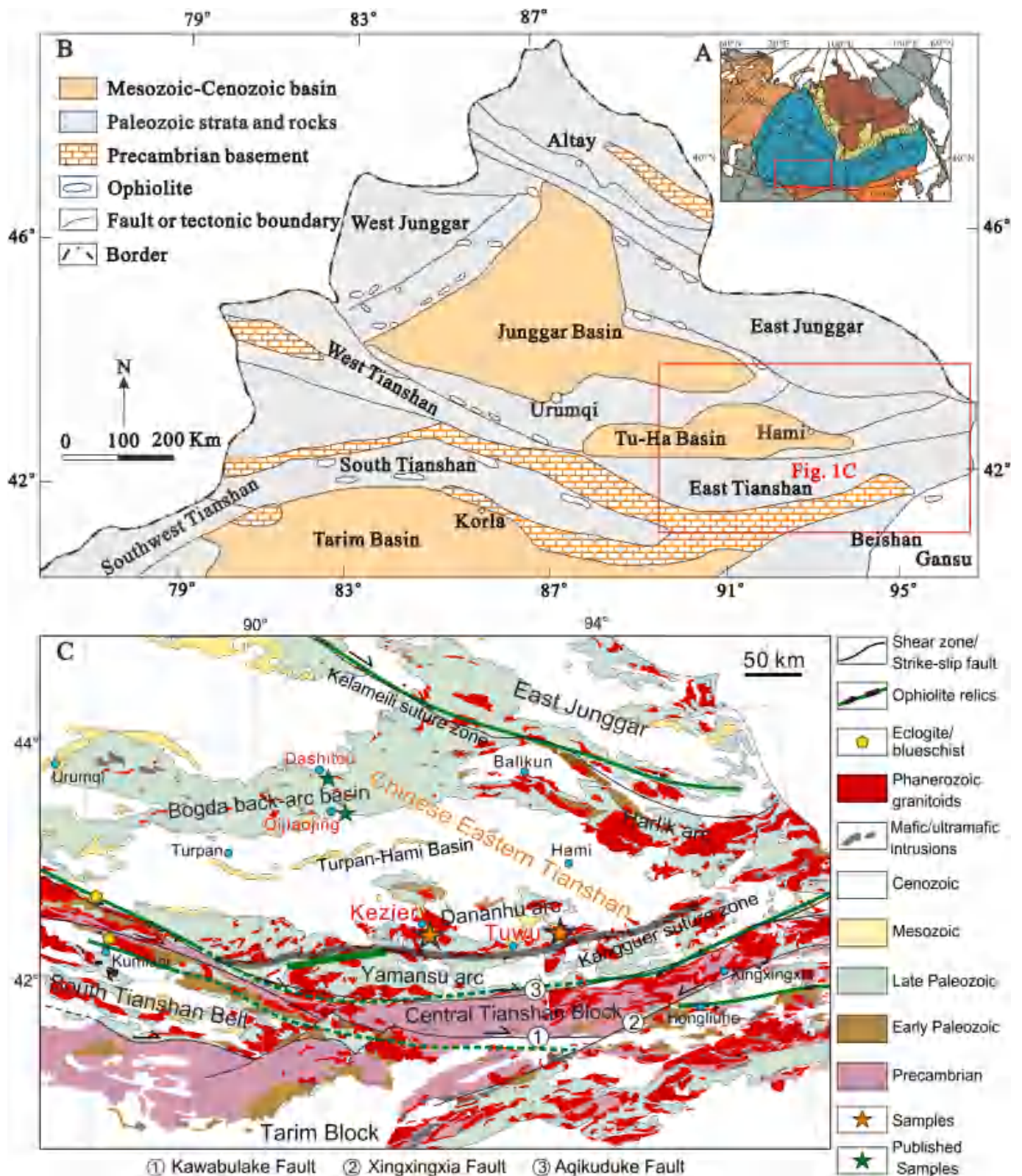

Fig. 1. (A) Sketch map of the CAOB and the adjacent area (after Jahn et al., 2000). (B) Sketch map of the North Xinjiang (modified from Gao et al., 2009). (C) Geological map of the Eastern Tianshan (after Han and Zhao, 2018).

consumption of various oceanic basins (Fig. 1A; Jahn et al., 2000; Windley et al., 2007). The Proterozoic to Paleozoic multi-stage tectonic evolution of oceanic basins in CAOB caused a huge system of orogenic collages formed by long-lived patchwork of different tectonic units (Wilhem et al., 2012; Windley et al., 2007; Zhang et al., 2022a, 2022b).

As one of the main mountain ranges of the CAOB, the Tianshan Orogen occupies the southern part of the CAOB and extends for over 2400 km from Uzbekistan to northern Xinjiang in China (Charvet et al., 2007; Han and Zhao, 2018). The Tianshan Orogen was formed by the Paleozoic evolution of the Paleo-Tianshan Ocean, and probably experienced
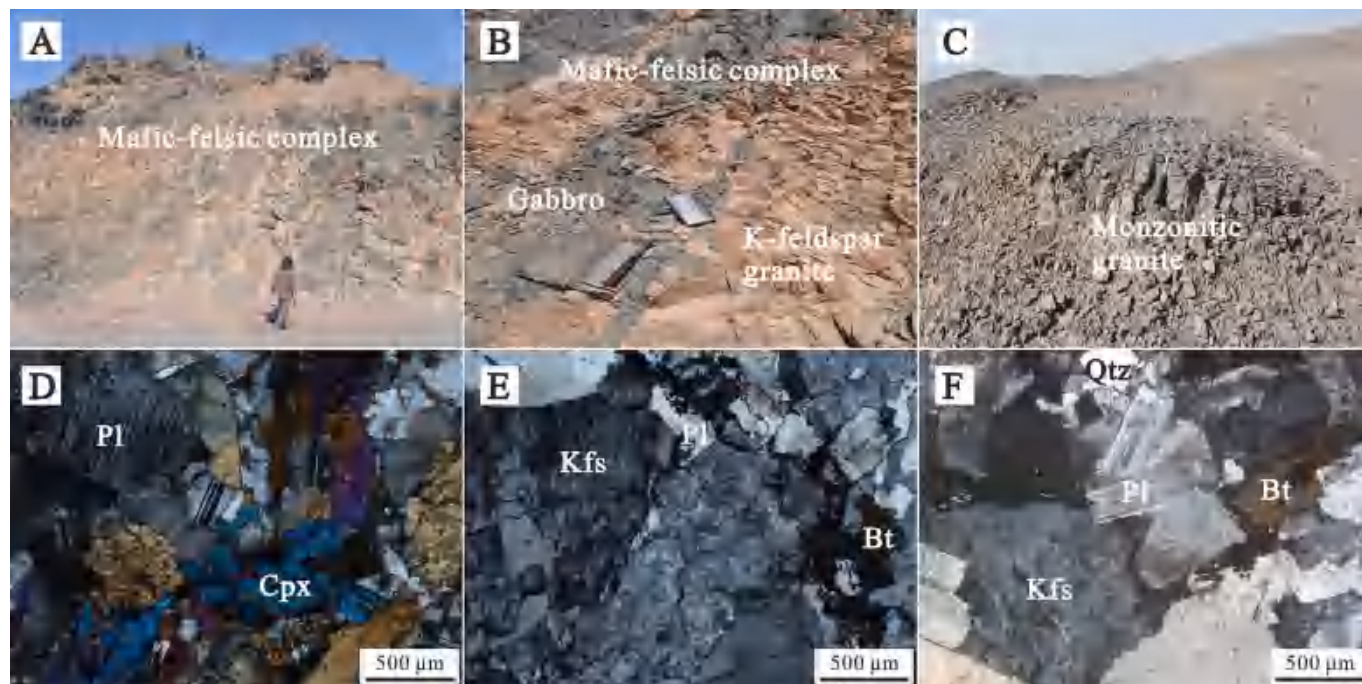
Fig. 2. Representative photographs and microphotographs of the Kezier mafic-felsic complex and Tuwu pluton in the Eastern Tianshan. (A and B) Photographs of outcrops for the Kezier complex; (C) Photograph of outcrop for the Tuwu monzonitic granitic pluton; (D and E) Microphotographs for the gabbro and K-feldspar granite from the Kezier complex, respectively; (F) Microphotograph for the monzonitic granite. Abbreviations: Cpx, clinopyroxene; Pl, plagioclase; Kfs, K-feldspar; Bt, biotite; Qtz, quartz.

multiple episodic arcs and back-arc basins (Charvet et al., 2007; Han and Zhao, 2018; Tao et al., 2022; Xiao et al., 2004; Zhang et al., 2018), and thus provides an excellent opportunity for us to characterize the tectonic transition from arc to back-arc basin. In fact, debate on these tectonic transitions of the Tianshan Orogen still exists, especially regarding the eastern part of the Tianshan Orogen–Chinese Eastern Tianshan, where records of high-grade metamorphism and deformation are sparse (Gao et al., 2009; Shu et al., 2011; Wang et al., 2014; Xiao et al., 2004). On the other hand, Paleozoic arc magmatism in the Eastern Tianshan is chronologically continuous and spatially widespread, and in particular, distinctly different distribution range and geochemical compositions of the arc magmatic rocks before and after Late Devonian were found in the Eastern Tianshan, probably indicating the initial structural change (e.g., Du et al., 2019, 2021; Mao et al., 2022; Wang et al., 2021; Zhang et al., 2018; Zhang et al., 2022a, 2022b). To date, however, the earliest solid evidence for tectonic extensional setting in the Eastern Tianshan were the Early Carboniferous (ca. 345 Ma and 330 Ma) back-arc basin-related bimodal volcanics (Chen et al., 2013; Zhang et al., 2017). In the absence of evidence for the pre-Carboniferous tectonic extensional setting in the Eastern Tianshan, which hindered the understanding of the tectonic switching between phases of trench retreat and advance and the Paleozoic arc–back-arc system evolutionary history in the Eastern Tianshan.

Accordingly, we conducted geochronological, bulk rock geochemical, and Sr—Nd isotopic analyses for the Late Devonian gabbros and granites from the Chinese Eastern Tianshan. Combined with contemporaneous geological events and available data from adjacent regions, new back-arc basin-related magmatism belts with pre-Carboniferous ages are recognized, and the timing and origin of these magmatic activities shed light on the tectonic transition from subduction to back-arc in the Chinese Eastern Tianshan.

2. Geological background and sample description

2.1. Geological background

The Chinese Tianshan is separating the Junggar terrane to the north from the Tarim Craton to the south (Fig. 1B), is a complex collage of island arc–back arc assemblages, oceanic remnants, accretionary complexes, and continental fragments (Charvet et al., 2007; Windley et al., 1990; Xiao et al., 2004). It can be geographically divided into the Eastern and Western Tianshan by a transect roughly along the Urumqi–Korla road (Fig. 1B). This study concentrates on the Eastern Tianshan, the framework of which is characterized by two major arc–back-arc systems (i.e., the Yamansu–Central Tianshan system and the Dananhu–Bogda–Harlik system in the south and north, respectively) separated by the Kangguer suture (Fig. 1C; Xiao et al., 2004; Charvet et al., 2007; Zhang et al., 2018; Wang et al., 2021; Zhang et al., 2022a, 2022b).

The Kangguer suture zone is mainly occupied by Carboniferous volcanic rocks, granitic intrusions and sedimentary, while Devonian magmatic rocks and ophiolite fragments are locally exposed (Du et al., 2019; Wang et al., 2014; Xiao et al., 2004). Ophiolites are made up of serpentinized peridotites, metabasalts, and gabbros, the ages for the gabbros were suggested to be 330–494 Ma, which represent remnants of the Kangguer oceanic plate (Du et al., 2019; Li et al., 2008; Wang et al., 2022). To the south of the Kangguer suture, the Yamansu belt predominantly contains Carboniferous marine strata and arc-related volcanic rocks, including basalts, andesites, and pyroclastic rocks, and were intruded by numerous granitoids (e.g., Du et al., 2018; Zhang et al., 2020). The Central Tianshan Block consists mainly of Proterozoic amphibolite-facies metamorphic basement and is overlain by Paleozoic assemblages of ultramafic to felsic volcanic rocks, granitoids, graywackes and flysch rocks (e.g., Huang et al., 2017; Ma et al., 2015). In addition, the basement of the Yamansu belt has been assigned to a close affinity to the Central Tianshan Block on the basis of the inherited zircon age peaks from the Carboniferous volcanic rocks and granitoids in the
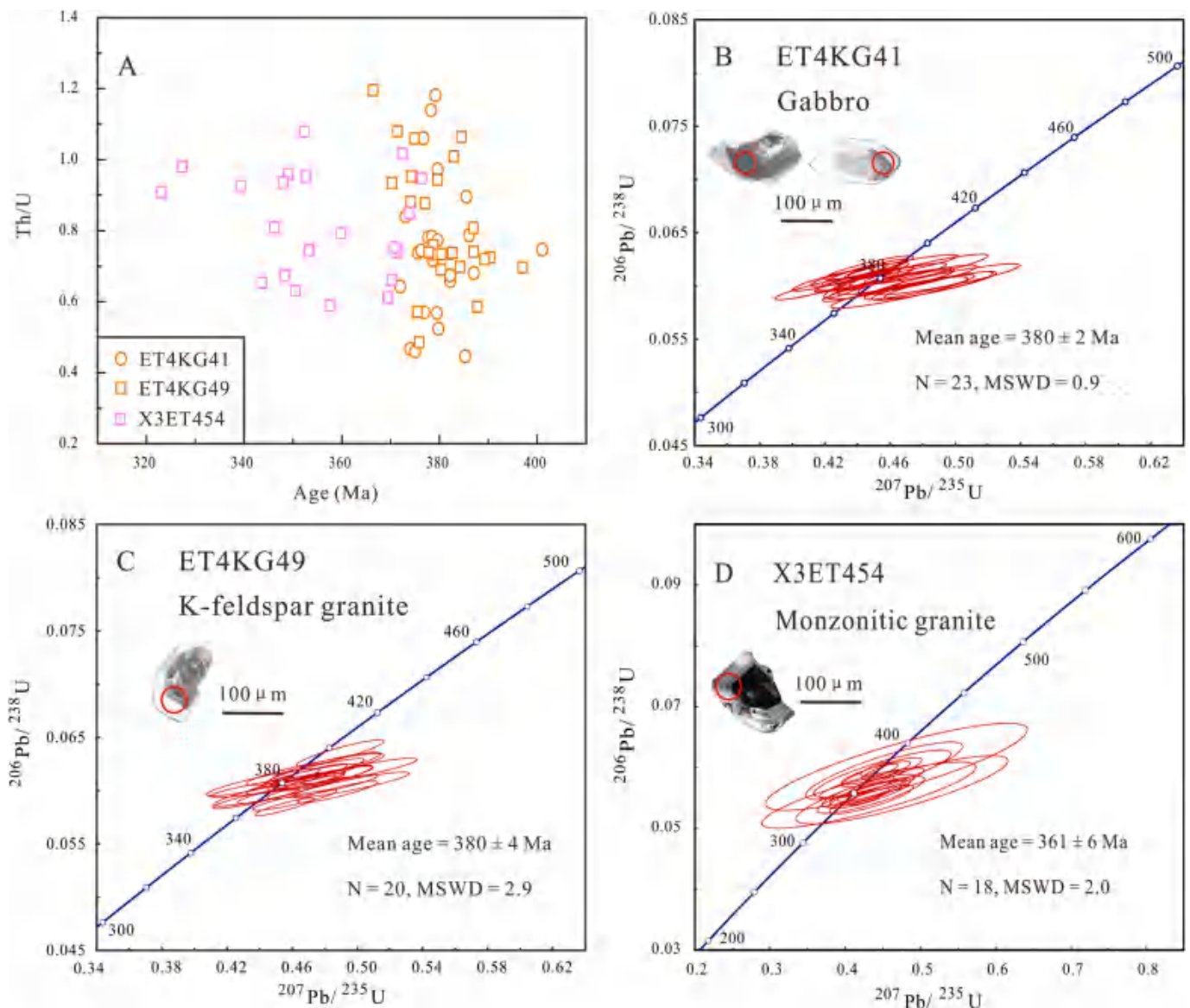
Fig. 3. Th/U versus age diagram of zircons for the gabbro and granites (A), and zircon U—Pb concordia diagrams for (B) sample ET4KG41 from the gabbro, (C) sample ET4KG49 from the K-feldspar granite, and (D) sample X3ET454 from the monzonitic granite. MSWD, mean square of weighted deviates.

Yamansu belt (Long et al., 2020; Luo et al., 2012), as well as the distinct zircon age cluster of detrital zircons from sandstones in the southern Kangguer and Yamansu belts (Chen et al., 2019). As a consequence, the Yamansu belt is envisaged as an Early Carboniferous continental marginal arc associated with southward subduction of the Kangguer oceanic plate (Chen et al., 2019; Du et al., 2021; Zhang et al., 2018). Subsequently, an extension of the overlying Yamansu arc crust and a tectonic transition from subduction to back-arc setting in the Late Carboniferous is favored to account for the regional structural, sedimentation, and magmatism (e.g., Du et al., 2021; Zhang et al., 2018).

To the north of the Kangguer suture belt, the other arc–back-arc assemblage is proposed, including the Ordovician to Carboniferous Dananhu–Harlik island arc and an intervening Bogda back-arc basin (Chen et al., 2013; Xiao et al., 2004; Zhang et al., 2017). The Ordovician to Silurian Huangcaopo Group in the Harlik terrane consist mainly of marine clastics and tuffs (Ma, 1999), and are predominantly overlain by Devonian to Permian flysch and clastic sediments, intercalated with minor volcaniclastic and volcanic rocks (Deng et al., 2016; Ma, 1999). While the oldest sedimentary strata in the Dananhu terrane are Ordovician to Silurian Daliugou Group, which show similar depositional ages

to the Huangcaopo Group (Deng et al., 2016; Ma, 1999). They are overlain by Devonian volcanic and pyroclastic rocks, but are unconformably overlain by Carboniferous to Permian volcanic rocks (Deng et al., 2016; Gao et al., 2015). Furthermore, the Harlik and Dananhu arcs were characterized by prolonged Ordovician to Carboniferous island arc magmatism (e.g., Du et al., 2019, 2021; Mao et al., 2022; Zhang et al., 2018). The Bogda Mountains, located between the Dananhu and the Harlik arcs, have been regarded as an Early Carboniferous back-arc basin and consists mainly of Carboniferous and Permian strata (Chen et al., 2013; Zhang et al., 2017). The former contains littoral-neritic facies clastic sediments and biolimestone with some bimodal volcanic lavas, while the latter are dominated by terrestrial sandstone, conglomerate, and siliceous mudstone intercalated with bimodal volcanic suites (Shu et al., 2011).

2.2. Sample description

Samples investigated in this study include a mafic–felsic complex in the Kezier area (N 42°19′45.5″, E 91°48′15.2″) and a granitic pluton to the east of the Tuwu area (N 42°14′19.6″, E 93°19′28.8″), Dananhu belt
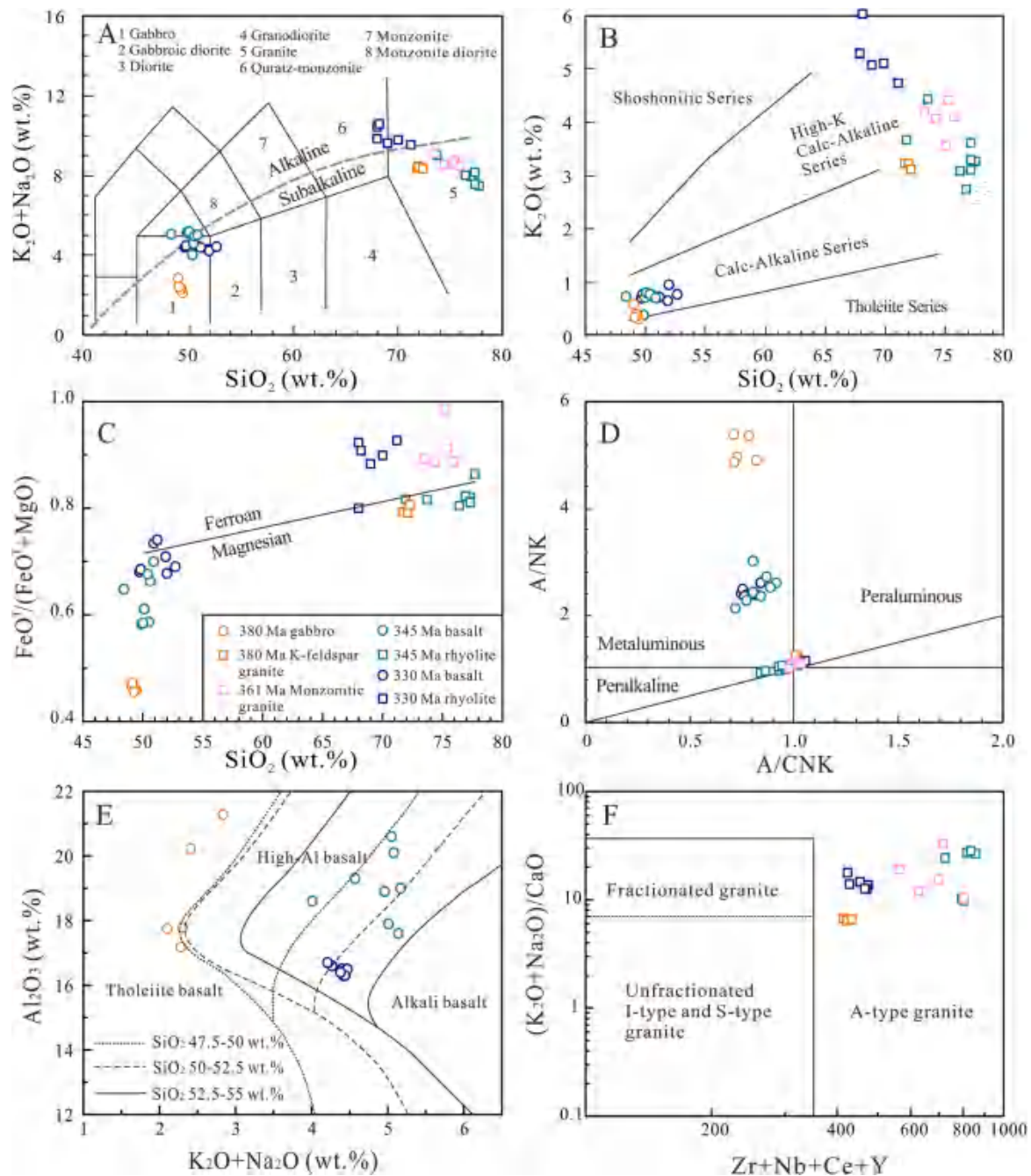
Fig. 4. (A) ($K_2O + Na_2O$) versus SiO_2 diagram. (B) K_2O versus SiO_2 diagram. (C) $FeO^T/(FeO^T + MgO)$ versus SiO_2 diagram. (D) A/NK versus A/CNK diagram. (E) Al_2O_3 versus ($K_2O + Na_2O$) diagram (after Kuno, 1960). (F) ($K_2O + Na_2O$)/CaO versus ($Zr + Nb + Ce + Y$) diagram (after Whalen et al., 1987). The data for the 345 Ma and 330 Ma bimodal volcanic rocks in the Bogda back-arc basin are from Chen et al. (2013) and Zhang et al. (2017), respectively.

(Fig. 1C). These rocks are undeformed, and fresh samples without recognizable alteration were collected for geochemical investigation. The Kezier gabbros from the complex are dark gray, massive, fine to medium grained, and show a gabbro texture with a mineral assemblage of plagioclase (45–60 vol%), clinopyroxene (30–40 vol%), and minor amphibole and Fe—Ti oxides (<5 vol%) (Fig. 2A, B, and D). The plagioclase and clinopyroxenes crystals show similar subhedral to euhedral with grain sizes of 0.2–1.0 mm (Fig. 2D). The Kezier K-feldspar granites from the complex are flesh pink, massive, medium to coarse grained, and mainly include K-feldspar (35–45 vol%), quartz (30–40%), plagioclase (10–15 vol%), biotite (~5 vol%), with minor accessory minerals (<5 vol%) (Fig. 2A, B, and E). The Tuwu monzonitic granites are light gray color with subhedral granular texture and mainly consist

of euhedral plagioclase (30–40 vol%), K-feldspar (30–35 vol%), and anhedral quartz (20–25 vol%), with minor biotite (~5 vol%) and accessory minerals (<5 vol%) (Fig. 2C and F).

3. Analytical results

Cathodoluminescence (CL) images of zircons were obtained at the State Key Laboratory of Isotope Geochemistry, Guangzhou Institute of Geochemistry, Chinese Academy of Sciences. Zircon U—Pb dating was performed at the School of Resources and Environmental Engineering, Hefei University of Technology. Whole-rock major and trace elements, and Sr—Nd isotopic analyses were measured at the Wuhan Sample So-lution Analytical Technology Co., Ltd. The details of analytical method
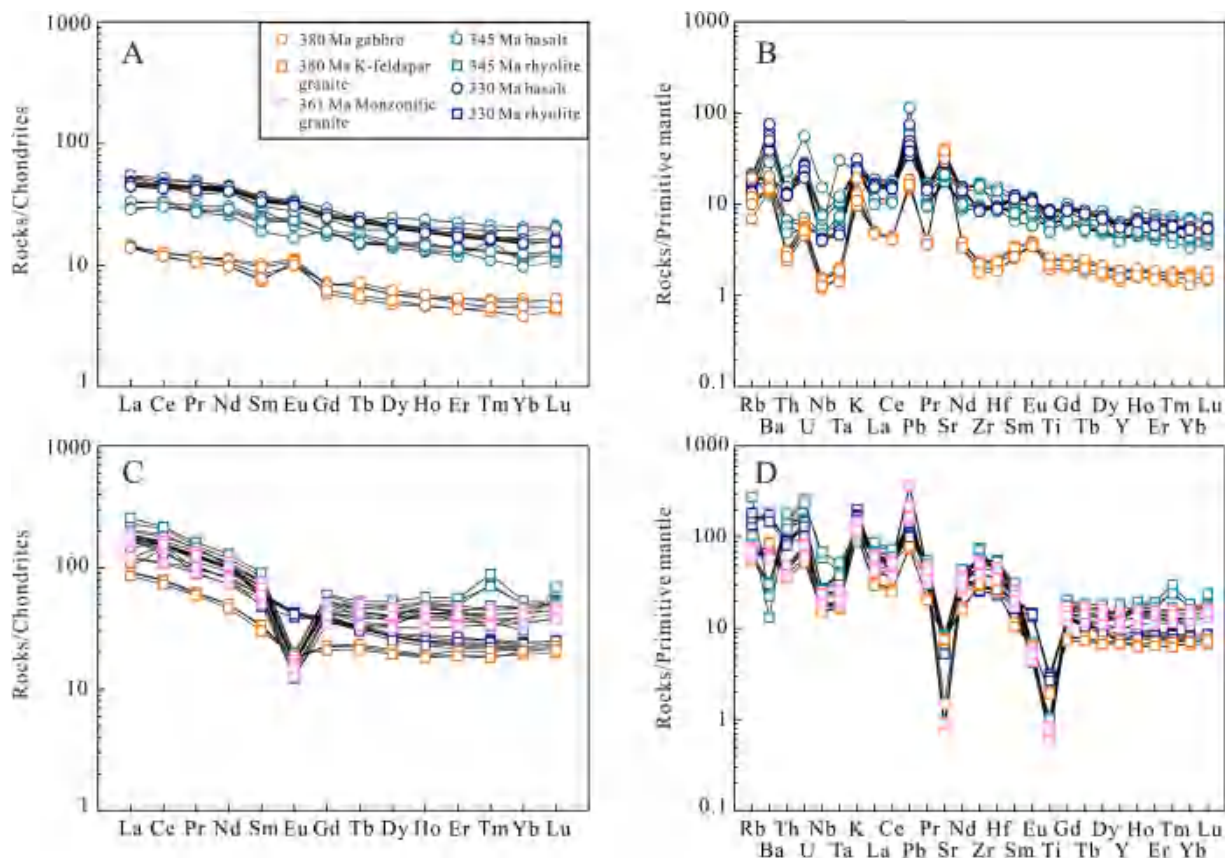
Fig. 5. Chondrite-normalized REE patterns and primitive mantle-normalized multi-element diagrams for the mafic rocks (A and B) and felsic rocks (C and D). Normalizing values are from Sun and McDonough (1989). The data for the 345 Ma and 330 Ma bimodal volcanic rocks in the Bogda back-arc basin are from Chen et al. (2013) and Zhang et al. (2017), respectively.

and results of this study are provided in Appendix.

3.1. Zircon geochronology

Sample ET4KG41 was collected from the gabbroic intrusion for geochronology analyses. Zircons from sample ET4KG41 are generally small and stubby (40–100 μm) with low length-to-width ratios (1:1–2:1). They show transparent, euhedral, and broadly concentric oscillatory zoning in CL images, which, combined with their high Th/U (0.45–1.18) ratios (Fig. 3A–B; Table S1), indicates a magmatic origin (e. g., Belousova et al., 2002). Among the 25 analyzed zircons, 23 analyses display a coherent group and yielded $^{206}Pb/^{238}U$ ages varying from 372 to 387 Ma, with a weighted mean age of 380 ± 2 Ma (Fig. 3B; Table S1). The other two analysis exhibit discordant $^{206}Pb/^{238}U$ age, probably due to Pb loss as a result of a thermal overprint.

Sample ET4KG49 from the K-feldspar granitic intrusion was chosen for zircon U—Pb analysis. The zircons separated from ET4KG49 are mostly transparent and prismatic and range from 50 to 150 μm with length/width ratios of 1:1 to 3:1 (Fig. 3C). They also have high Th/U (0.49–1.20) ratios (Fig. 3A; Table S1) and show magmatic oscillatory zoning, suggesting an igneous origin. Twenty of the 25 analyses of zircons display a coherent cluster with a weighted $^{206}Pb/^{238}U$ mean age of 380 ± 4 Ma (Fig. 3C; Table S1). Overall, the consistent zircon U—Pb dating results for the two samples (ET4KG41 and ET4KG49) suggest that the gabbroic and granitic complex formed in the Late Devonian.

Zircon grains from the monzonitic granite (X3ET454) are mostly prismatic crystals and transparent. They show length-to-width ratios of 1:1 to 2:1 with size ranging between 50 and 150 μm (Fig. 3D). They exhibit similar characteristics to magmatic zircons with high Th/U (0.59–1.08) ratios (Fig. 3A; Table S1) and distinct oscillatory zoning.

Among the 22 analyzed zircons, four analyses of zircons plot away from the Concordia curve due to partial Pb loss. The others yielded a weighted $^{206}Pb/^{238}U$ mean age of 361 ± 6 Ma (Fig. 3D; Table S1). Hence, the emplacement era of the monzonitic granitic intrusion was also Late Devonian.

3.2. Whole-rock geochemistry

The gabbroic samples from the Kezier mafic–felsic complex possess relatively low SiO_2 (49.1–49.5 wt%), TiO_2 (0.42–0.57 wt%), K_2O (0.29–0.57 wt%), and total alkali ($K_2O + Na_2O = 2.10$–2.84 wt%), but show high CaO (11.3–12.1 wt%), MgO (6.31–9.04 wt%), $Fe_2O_3^T$ (6.10–8.43 wt%), and $Mg^{\#}$ (67–68) values (Fig. 4A, B; Table S2). Accordingly, they exhibit magnesian and metaluminous characteristics as manifested by their low $FeO^T/(FeO^T + MgO)$ (0.46–0.47) and A/CNK (molar $Al_2O_3/(CaO + Na_2O + K_2O)$, 0.71–0.82) values (Fig. 4C, D; Table S2). It is worth noting that these samples are characterized by relatively high Al_2O_3 (17.2–21.3 wt%) contents, similar to the high-Al basalt and basaltic andesite defined by Kuno (1960; Fig. 4E). The gabbros have relatively high contents of transition elements, for example, Cr (138–181 ppm) and Ni (52.3–79.0 ppm) (Table S2). They display moderate LREE (light rare earth element) enrichment (($La/Yb)_N$ = 2.70–3.73) and weakly fractionated HREE (heavy rare earth element; $(Gd/Yb)_N$ = 1.32–1.56) with slightly positive Eu anomalies (Eu/Eu* = 1.29–1.68) (Fig. 5A; Table S2). On the primitive mantle-normalized trace element diagram (Fig. 5B), these rocks show relative enrichment in LILEs (large ion lithophile elements; e.g., Ba, U, and Sr), and depletion in HFSEs (high field strength elements; e.g., Nb and Ta). The samples have consistent initial $^{87}Sr/^{86}Sr$ ratios (0.7034–0.7035), with depleted $\varepsilon_{Nd}(t)$ values (6.13–6.96) and juvenile two stage Nd model ages (T_{DM}^2 =
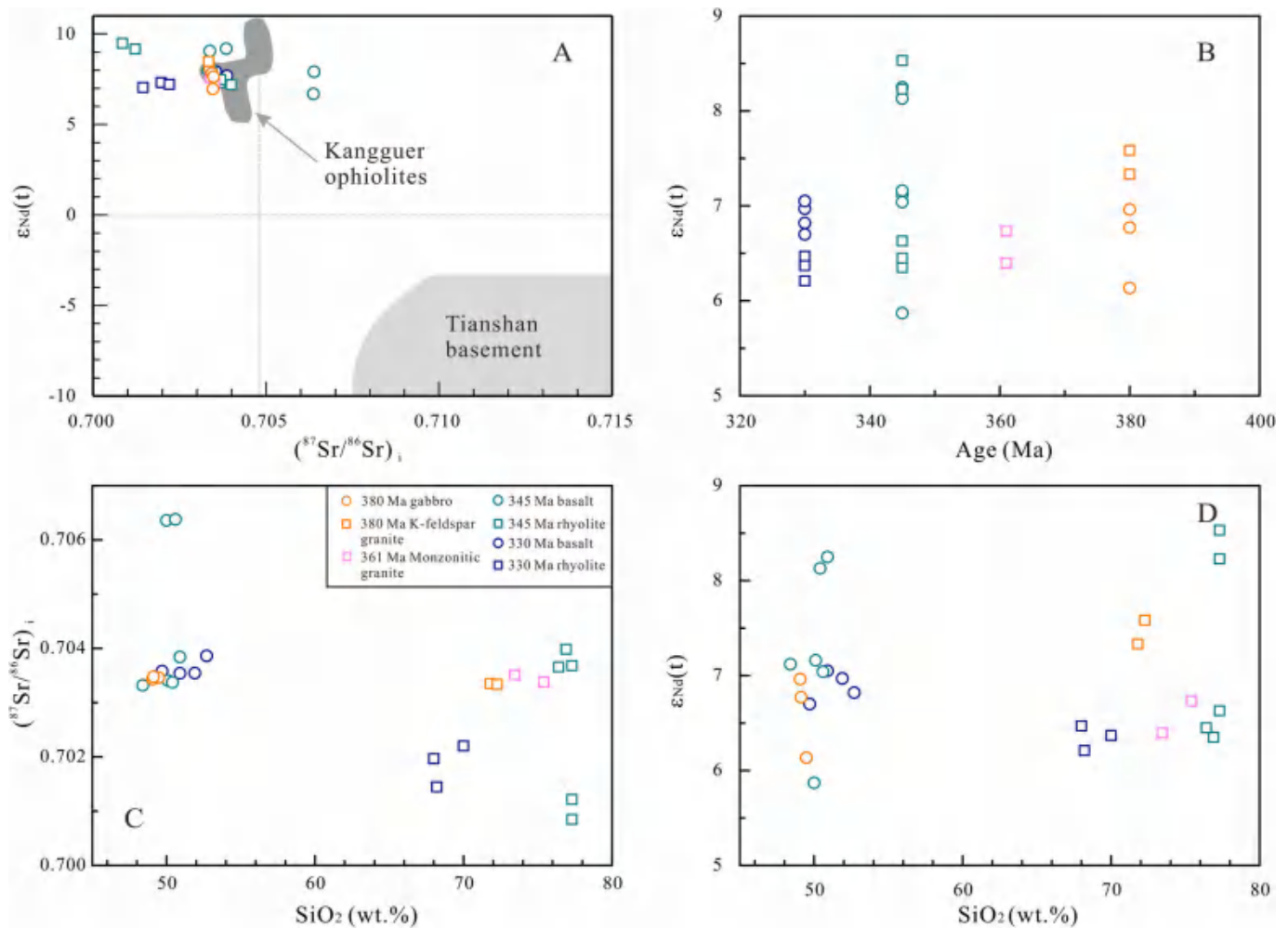
Fig. 6. (A) $\varepsilon_{Nd}(t)$ versus $(^{87}Sr/^{86}Sr)_i$ diagram. (B) $\varepsilon_{Nd}(t)$ versus age diagram. (C) $(^{87}Sr/^{86}Sr)_i$ versus SiO_2 diagram. (D) $\varepsilon_{Nd}(t)$ versus SiO_2 diagram. The range of the Kangguer ophiolites and Tianshan basement are from Li et al. (2008) and Tang et al. (2014), respectively. The data for the 345 Ma and 330 Ma bimodal volcanic rocks in the Bogda back-arc basin are from Chen et al. (2013) and Zhang et al. (2017), respectively.

564 to 633 Ma) (Fig. 6A; Table S3).

The K-feldspar granitic samples from the Kezier mafic–felsic complex have high SiO_2 (71.8–72.3 wt%), K_2O (3.09–3.21 wt%), and Na_2O (5.06–5.19 wt%) contents, but display low Al_2O_3 (14.3 wt%), $Fe_2O_3^T$ (2.20–2.32 wt%), MgO (0.50–0.53 wt%), and $Mg^\#$ (30–32) values (Table S2). They plot within the granite and calc-alkaline field, and belong to the magnesian and weakly peraluminous series as illustrated by their low $FeO^T/(FeO^T + MgO)$ (0.79–0.81) and A/CNK (1.00–1.01) values (Fig. 4A–D; Table S2). These samples exhibit remarkably LREE enriched patterns $((La/Yb)_N = 4.17$–4.80), with flat HREE patterns $((Gd/Yb)_N = 1.02$–1.17) and Eu negative anomalies (Eu/Eu* = 0.67–0.75) (Fig. 5C). The primitive mantle-normalized trace element diagram show that they are enriched in Rb, U, and Pb, but depleted in Th, Nb, Ta, Sr, and Ti (Fig. 5D). Moreover, these rocks contain high Zr (325–346 ppm), Nb (11.0–11.9 ppm), Ce (44.4–48.6 ppm), Y (30.7–33.6 ppm) and Ga (17.1–17.3 ppm) concentrations (Table S2), making them akin to A-type granites described by Whalen et al. (1987). The K-feldspar granites have changeless initial $^{87}Sr/^{86}Sr$ ratios (0.7033–0.7034), and show slightly higher $\varepsilon_{Nd}(t)$ values (7.33–7.58) and more juvenile T_{DM}^2 ages (512 to 533 Ma) than those of the gabbros from the same complex (Fig. 6A–D; Table S3).

Relative to the K-feldspar granites, the monzonitic granitic rocks from the east of the Tuwu area also characterized by high SiO_2 (73.4–75.9 wt%), K_2O (3.55–4.42 wt%), and Na_2O (4.32–5.01 wt%) concentrations, with low Al_2O_3 (12.2–13.8 wt%), $Fe_2O_3^T$ (1.35–2.25 wt

%), MgO (0.03–0.22 wt%), and $Mg^\#$ (3–19) values (Fig. 4A, B; Table S2). However, they possess slightly higher $FeO^T/(FeO^T + MgO)$ (0.89–0.98) and more scattered A/CNK (0.97–1.03) values (Fig. 4C, D; Table S2). Both types of granites show LREE enriched patterns, with unfractionated HREE and Eu negative anomalies (Fig. 5C). The monzonitic granites as well display pronounced spikes of Rb, U, and Pb, and troughs of Th, Nb, Ta, Sr, and Ti (Fig. 5D). More importantly, their geochemical characteristics are also similar to those of typical A-type granites, such as high Zr (439–621 ppm), Nb (13.3–17.5 ppm), Ce (65.9–100 ppm), Y (45.8–66.3 ppm) and Ga (23.3–24.5 ppm) contents (Whalen et al., 1987; Fig. 4F; Table S2). In addition, the monzonitic granitic samples have consistent initial $^{87}Sr/^{86}Sr$ ratios (0.7034–0.7035) and depleted $\varepsilon_{Nd}(t)$ values (6.39–6.73), with juvenile T_{DM}^2 ages (568 to 596 Ma) (Fig. 6A–D; Table S3).

4. Discussion

4.1. Geochronological framework of the extensional setting magmatism

Late Carboniferous to Early Permian (ca. 310–280 Ma) post-collisional extensional structures and magmatism widely occur in the Eastern Tianshan orogenic belt, such as Balikun Nb-enriched gabbros and A-type granites in the Harlik belt (Yuan et al., 2010), Qijiaojing bimodal volcanic rocks and Hongshankou Nb-enriched dolerites in the Bogda belt (Zhang et al., 2020), Sha'erhu A-type granites in the
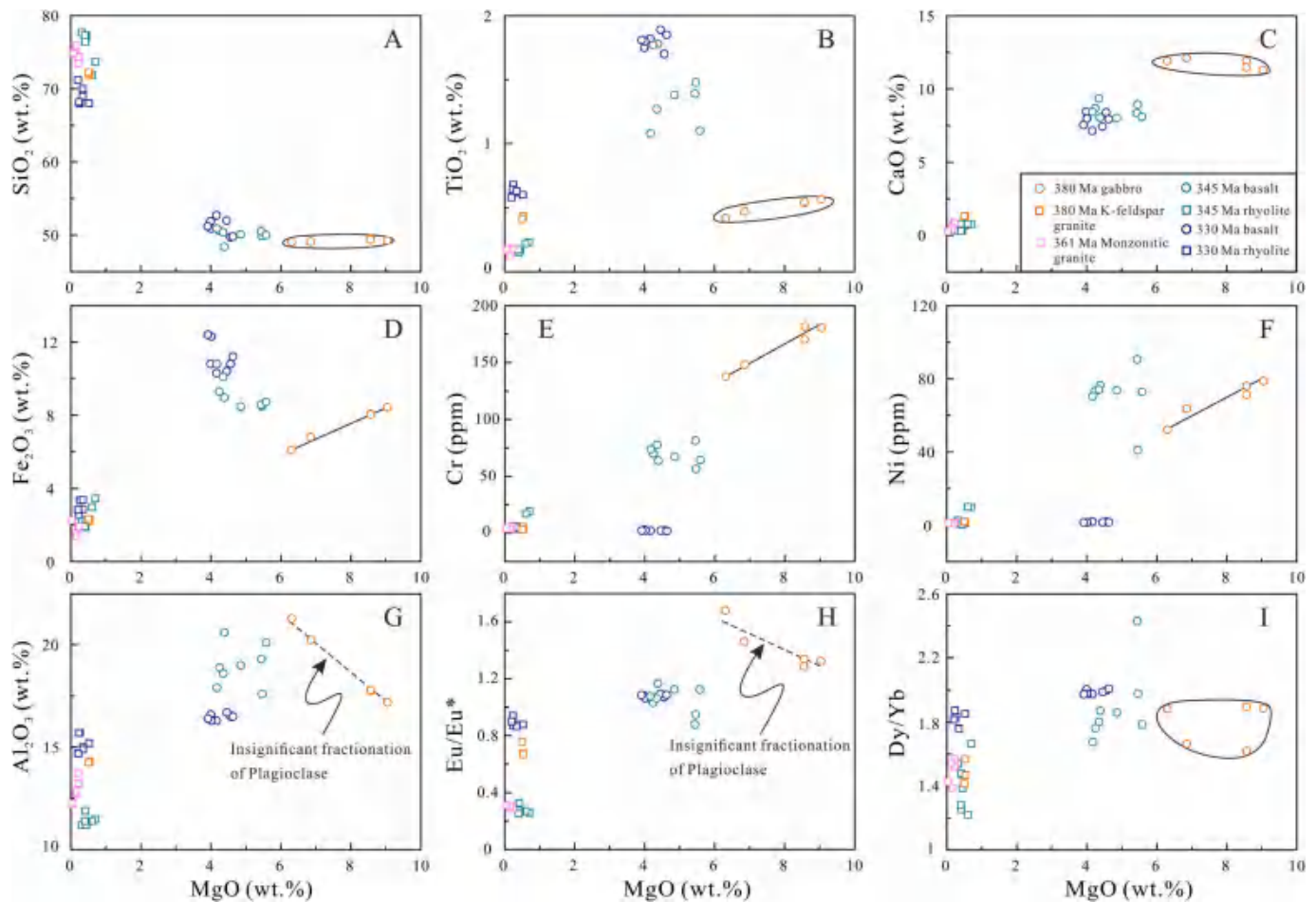
Fig. 7. Variations of selected major and trace element contents and ratios versus MgO for the rocks in the Eastern Tianshan. The data for the 345 Ma and 330 Ma bimodal volcanic rocks in the Bogda back-arc basin are from Chen et al. (2013) and Zhang et al. (2017), respectively.

Dananhu belt (Mao et al., 2014), mafic-ultramafic rocks and shear zone-hosted Au deposits in the Kangguer belt (Qin et al., 2011; Xiao et al., 2004), and Dikan'er Nb-rich basalts and Aqishan mountain A-type granites in the Yamansu belt (Du et al., 2018; Zhang et al., 2020), etc.

So far, however, the earlier extensional magmatism (e.g., ca. 345 Ma Heishankou bimodal volcanism and ca. 330 Ma Dashitou bimodal volcanism) only have been identifed in the Bogda belt (Chen et al., 2013; Zhang et al., 2017). Previous studies proposed that these bimodal rocks were probably related to a back-arc setting based on they show both intraplate- and arc-like magmatic affinities, and the regional sedimentation, as well as the distribution of magmatism in the adjacent area (Chen et al., 2013; Du et al., 2021; Zhang et al., 2017, 2018). Here, we report newly identifed Late Devonian (380–361 Ma) extensional magmatism (high-Al gabbros + A-type granites) in the Dananhu belt, the Dananhu–Bogda–Harlik system. Combined with previously published data of the Early Carboniferous bimodal volcanism (Chen et al., 2013; Zhang et al., 2017), we are trying to provide new evidence for the Paleozoic evolutionary history of the Dananhu–Bogda–Harlik arc–back-arc system.

4.2. Petrogenesis of the high-Al gabbros

4.2.1. Effects of alteration, crustal assimilation, and fractional crystallization

The high-Al gabbros from the Kezier mafic–felsic complex show well preserved primary minerals (e.g., clinopyroxene and plagioclase) with slight alteration and low LOI (loss on ignition) values (<1.89 wt%) (Fig. 2D and Table S2), implying that late alteration did not significantly influence their original magmatic compositions. This is consistent with the observation that their LILE contents and isotope compositions do not correlate with their LOI values. It is also important to consider the possible effects of shallow level processes such as crustal contamination and fractional crystallization. Commonly, crustal materials are characterized by low Nb/La, Nb/Th, and $\varepsilon_{Nd}(t)$ but high $^{87}Sr/^{86}Sr$ ratios (Rudnick and Fountain, 1995), and thus crustal contamination will cause decreases in Nb/La, Nb/Th, and $\varepsilon_{Nd}(t)$ but an increase in initial $^{87}Sr/^{86}Sr$ ratios. In fact, the basic rocks have relatively limited ranges in SiO_2 contents (49.1–49.5 wt%), $Mg^{\#}$ values (67–68), and Sr isotopic compositions (0.7034–0.7035), as well as constant Nb/La (0.25–0.33) and Nb/Th (4.03–4.62) ratios (Fig. 6A, B; Tables S2 and S3), which are inconsistent with crustal assimilation (Rudnick and Gao, 2003). Furthermore, the Kezier gabbros and granites show consistent initial $^{87}Sr/^{86}Sr$ ratios, but gabbros display lower Nd isotopic ratios than the granites (Fig. 6C, D), which is the converse of what would be expected from crustal contamination. Instead, a mantle component played a prominent role in their genesis.

The Late Devonian gabbros in this study possess relatively evolved Cr (138–181 ppm) and Ni (52.3–79.0 ppm) concentrations, which are lower than those of primary mantle-derived magmas (e.g., Cr = 300–500 ppm, Ni = 300–400 ppm; Frey et al., 1978), suggesting that their parental magmas experienced various degrees of differentiation. Actually, they show constant SiO_2, TiO_2, and CaO contents (Fig. 7A–C) clearly imply negligible degrees of fractionation. Although their MgO contents positively correlate with $Fe_2O_3^T$, Cr, and Ni contents (Fig. 7D–F), possibly due to removal of olivine and clinopyroxene during magma ascent. Conversely, the positive Eu and Sr anomalies, together with the
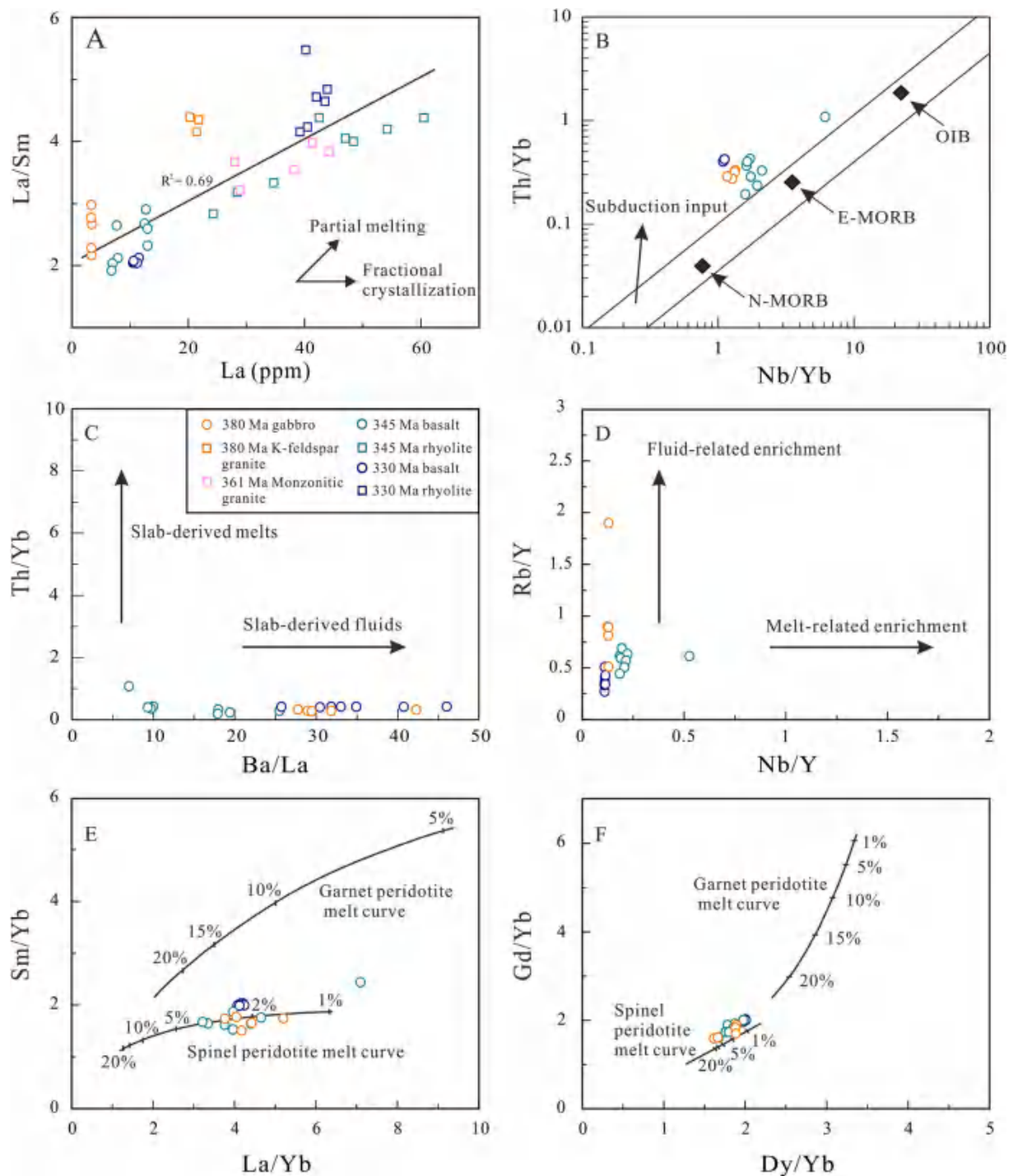
Fig. 8. (A) La/Sm versus La plot (after Allegre and Minster, 1978). (B) Th/Yb versus Nb/Yb plot for the mafic rocks (after Pearce, 2008). N-MORB, normal mid-ocean-ridge basalt; *E*-MORB, enriched mid-ocean-ridge basalt; OIB, oceanic-island basalt. (C) Th/Yb versus Ba/La plot for the mafic rocks (after Woodhead et al., 2001). (D) Rb/Y versus Nb/Y plot for the mafic rocks (after Wang et al., 2014). (E) Sm/Yb versus La/Yb plot for the mafic rocks (after Zhao and Zhou, 2009). (F) Gd/Yb versus Dy/Yb plot for the mafic rocks (after Tang et al., 2014). The data for the 345 Ma and 330 Ma bimodal volcanic rocks in the Bogda back-arc basin are from Chen et al. (2013) and Zhang et al. (2017), respectively.

negative correlation of Al_2O_3 and Eu/Eu* with MgO (Figs.5A–B and 7G–H), argue against plagioclase fractionation. Because amphibole preferentially incorporates MREE compared to HREE, the identical Dy/Yb ratios for the gabbros (Fig. 7I) clearly indicate negligible amphibole fractionation. In summary, these rocks were most likely formed through olivine and clinopyroxene fractionation from primary mantle-derived basaltic magmas. Compared to the Early Carboniferous basalts in the Bogda belt, they have similar Sr—Nd isotopic compositions

(Fig. 6; Chen et al., 2013; Zhang et al., 2017), suggesting that they probably are petrogenetically related. Moreover, these samples show variable La/Sm ratios associated with the La contents (Fig. 8A), which indicates that the effects of partial melting and source compositions were more important than fractional crystallization. Hence, the distinctive geochemical composition of the samples from different eras could result from different degree of partial melting or heterogeneity in their mantle sources.
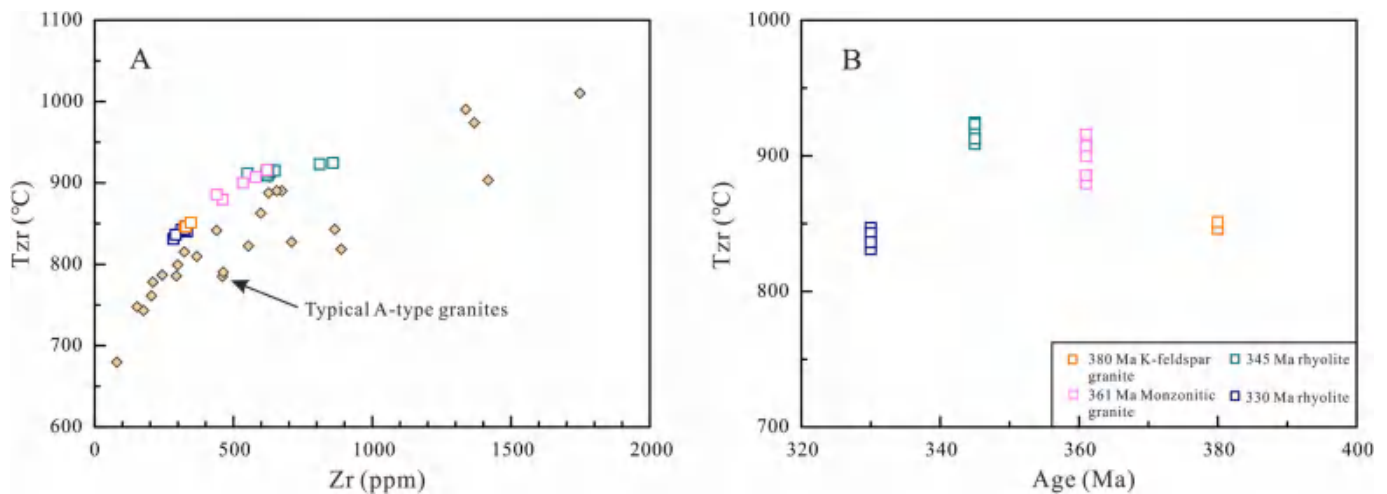
Fig. 9. (A) T_{Zr} (zircon saturation temperature) versus Zr content plot for the felsic rocks. (B) T_{Zr} versus age plot for the felsic rocks. The typical A-type granites are from Whalen et al. (1987). The data for the 345 Ma and 330 Ma rhyolites in the Bogda back-arc basin are from Chen et al. (2013) and Zhang et al. (2017), respectively.

4.2.2. Nature of the mantle source

The Late Devonian gabbros are characterized by relatively high Al_2O_3 contents (17.2–21.3 wt%), making them akin to high-Al basalt defined by Kuno (1960; Fig. 4E). Although previous studies suggest that high-Al basalt could be generated by high-degree partial melting of subducted slab material (Johnson, 1986), the modeling work implies that basalt-eclogite melting cannot yield major element compositions analogous to the high-Al basalt (Crawford et al., 1987). The flat chondrite-normalized HREE patterns of the high-Al samples ($(Gd/Yb)_N$ = 1.32–1.56) also preclude an eclogite source, since partial melting of eclogite with residual garnet would produce significant HREE depletions (Sisson and Grove, 1993). Other proposed mechanisms for the origin of high-Al magmas include preferential accumulation of plagioclase during the evolution of basaltic magma (e.g., Crawford et al., 1987; Wagner et al., 1995) or delayed plagioclase nucleation (e.g., Crawford et al., 1987; Sisson and Grove, 1993). However, Beard and Lofgren (1992) argued that plagioclase accumulation is not necessarily required to explain the petrogenesis of high-Al rocks. This, together with the positive Eu and Sr anomaly and the relationship between Al_2O_3 or Eu/Eu* with MgO of the studied samples (Figs. 5A–B and 7G–H), argues against the role of accumulation of plagioclase in the genesis of the studied gabbros. Instead, it is now generally accepted that the key factor for the high alumina feature is the delayed plagioclase crystallization under either hydrous or high pressure conditions (e.g., Xie et al., 2016; Xu et al., 2020).

The depleted Sr—Nd isotopic compositions, together with the low Th (0.20–0.26 ppm) and Th/La ratios (0.06–0.08) of the gabbros (Fig. 6A; TableS2) imply that they were originated from a depleted mantle source. Actually, the enrichments of LILE relative to HFSE with remarkable Nb—Ta anomalies are indicative of some characteristics of arc-related magmatism and reflect a depleted mantle source previously hybridized by fertile mantle components in a subduction zone (Pearce et al., 2005). The fertile mantle components in mafic magma are generally attributed to OIB involvement (Márquez et al., 1999) or asthenosphere upwelling metasomatised by enriched materials (Ferrari, 2004). While their Ta/Yb (0.07–0.10), Nb/Ta (13.0–15.7), Nb/La (0.25–0.33), and Nb/Yb (1.16–1.33) ratios are significantly lower than those of OIB (e.g., Hofmann, 1997), together with flat HREE patterns, implying that they were unlikely derived from an OIB-like mantle source. Instead, on a Th/Yb versus Nb/Yb diagram (Fig. 8B), all the mafic rocks plot above the MORB–OIB array, suggesting the involvement of a subduction related enriched materials (Pearce, 2008). Subduction related fertile components generally include slab-derived fluid or melt, and the addition of

different materials would cause different geochemical signatures on the magmas (Long et al., 2020; Sun and McDonough, 1989). Subduction zone fluid is enriched in highly mobile elements (e.g., Rb, Ba, and Pb) due to the low temperature dehydration at shallow levels. Then, partial melting of mantle metasomatised by such fluid would generate magmas with high mobile element/ immobile element ratios, such as Ba/La and Rb/Y ratios (Long et al., 2020; Pearce et al., 2005; Wang et al., 2014). Nevertheless, partial melting of mantle metasomatised by slab-derived melts at deeper depths with high temperature would yield high Th/Yb and Nb/Y ratios (Long et al., 2020; Pearce et al., 2005; Wang et al., 2014). The high contents of highly mobile elements such as Rb, Ba, and Pb of the gabbroic samples (Table S2) imply the involve of slab-derived fluids. Furthermore, their high and variable Ba/La (27.7–42.2) and Rb/Y (0.51–1.90) but low and constant Th/Yb (0.27–0.33) and Nb/Y (0.12–0.13) ratios (Fig. 8C–D; Table S2) as well argue for that the subduction components were dominated by hydrous fluids instead of melts (Wang et al., 2014; Woodhead et al., 2001).

The melting depths of the gabbros can be modeled by using the related REE ratios, such as La/Yb, Sm/Yb, Dy/Yb, and Gd/Yb ratios, since different minerals exist at different depths and have different partition coefficients for these elements (Mckenzie, 1991). Garnet has a high partition coefficient for Yb, whereas La and Sm are incompatible and have almost the same partition (e.g., Johnson, 1994). Therefore, various degrees of partial melting of a garnet lherzolite source with garnet residue produce melts with significantly decreasing Yb and increasing La/Yb and Sm/Yb ratios than those in a garnet-absent mantle source. In the case of the gabbroic samples, they possess low Sm/Yb and La/Yb ratios, which plot along the melting curve of spinel peridotite (Fig. 8E), indicating that they were likely derived from a spinel-facies mantle. This interpretation is further manifested in the Gd/Yb–Dy/Yb modeling diagram (Fig. 8F). Similarly, garnet has a high partition coefficient for Yb relative to Gd and Dy, and thus partial melting of a garnet lherzolite mantle will cause strong fractionation of Dy/Yb and Gd/Yb (e.g., Johnson, 1994). By contrast, spinel has similar partition coefficients for Yb, Gd, and Dy, and thus Dy/Yb and Gd/Yb will be slightly fractionated during melting in the spinel stability field (Green, 2006). Generally, the rocks have relatively low Dy/Yb and Gd/Yb values, and they plotted in or near the spinel lherzolite melting curve (Fig. 8F), suggesting that partial melting took place at a relatively shallow depth, dominantly within the spinel stability field.

Collectively, we infer that the Late Devonian high-Al gabbros may have originated from a depleted mantle fluxed by fertile mantle components at shallow depths induced by an upwelling asthenosphere.

Further, the primary compositions of the mantle-derived magma were modified by the influence of slab-derived fluids, suggesting the high alumina in the studied samples due to delayed plagioclase crystallization under hydrous rather than high pressure condition.

4.3. Petrogenesis of the A-type granites

Both types of granites in this study are characterized by high contents of SiO_2, total alkali, Ga/Al, HFSE (e.g., Zr, Nb, and Y), and low abundances in MgO, CaO, Ba, Sr, and Ti, with negative Eu anomalies (Fig. 5C–D and Table S2). The above characteristics indicate that they are belong to A-type granites, as demonstrated in the $(K_2O + Na_2O)/CaO$ versus $Zr + Nb + Ce + Y$ plot (Fig. 4F; Whalen et al., 1987; Eby, 1992; Bonin, 2007). In addition, the granites in this study lack inherited zircon, then their zircon saturation temperature calculated from bulk rock compositions can be used to provide minimum estimate of the temperature of the initially emplaced magma (Watson and Harrison, 1983). Their high zircon saturation temperatures are also completely consistent with those of typical A-type granites (Fig. 9A; Whalen et al., 1987). Mechanisms involving partial melting of crustal sources (Whalen et al., 1987; Eby, 1990), fractional crystallization of mantle-derived magma (Bonin, 2007), or mixing between crust- and mantle-derived magma (Kemp et al., 2005), are often suggested to explain the petrogenesis of A-type magmas.

The rocks of the Kezier mafic–felsic complex show compositionally bimodal, coupled with the presence of negative Eu, Ba and Sr anomalies in the A-type granites (Fig. 5C, D), seems to indicate that the granites were generated by fractionation of the coeval basaltic magma, same as the proposed mechanism for the ca. 345 Ma Heishankou bimodal volcanism (Chen et al., 2013). However, the high SiO_2 (>71.8 wt%) and low MgO (<0.53 wt%) contents of the rocks imply that they were not directly derived from the upper mantle (Bonin, 2007). Moreover, these A-type granites formed at very high temperatures (up to 851 °C), suggesting that extensive fractional crystallization from mafic magma was not feasible. Due to the constant La and La/Sm values for the Kezier granites (Fig. 8A), the model of fractional crystallization from mantle-derived magma can further ruling out. Since the lack of inherited zircon or mafic microgranular enclaves in the samples, mixing of crust- with mantle-derived magma is not a plausible mechanism either (Zhang et al., 2017). They show changeless Sr—Nd isotopic compositions, with similar $^{87}Sr/^{86}Sr$ ratios but higher $\varepsilon_{Nd}(t)$ values than the coeval gabbros

from the same complex (Fig. 6), further reflect that these rocks cannot be produced by magma mixing. Instead, partial melting of the crust appears to be the probable mechanism for the Kezier A-type granites.

Generally, the mineral assemblages in crustal source rocks of the granites can be constrained by their geochemical features. The distinctly negative Eu and Sr anomalies, low Sr/Y and La/Yb ratios, and relatively flat HREE patterns of these A-type rocks (Fig. 5C–D and Table S2) likely reflect the presence of residual plagioclase but absence of garnet in their sources, which suggests the A-type magma generation under a pressure lower than 0.8–1.0 GPa (Patiño Douce and Beard, 1995; Xiong et al., 2005). Finally, the depleted Sr—Nd isotopes and juvenile T_{DM}^2 values of the Kezier A-type granites are obviously different from the Tianshan basement, but indistinguishable from the juvenile crust in the CAOB and the Kangguer ophiolites (Fig. 6A and Table S3), thus indicating they were probably orignated from high temperature melting (up to 851 °C) of a juvenile crustal source under a low-pressure (<0.8–1.0 GPa) condition, analogous to the proposed model for the ca. 330 Ma Dashitou A-type rhyolite (Zhang et al., 2017).

The Tuwu A-type granites have extremely similar element distribution patterns to the Kezier A-type granites (Figs. 4–5), indicating a close genetic link. Compared to the former, they show slightly less depleted Sr—Nd isotopic compositions but higher zircon saturation temperatures (Figs. 6B and 9B). Therefore, we infer that the Tuwu granites were also generated by partial melting of a crustal source at a low-pressure level, whereas they had undergone higher temperatures (up to 916 °C) and involvement of a little less proportion of juvenile material in their source.

4.4. Geodynamic implication

The northern arc system in the Eastern Tianshan, including the Dananhu and Harlik arcs, has been traditionally regarded as southward subduction of the Junggar Ocean, which was reinforced by subsequent researches on tectonism and sedimentation (Charvet et al., 2007; Zhang et al., 2016). Nonetheless, there has been increasing investigations revealed that the Kangguer oceanic plate initial northward subduction occurred during the Middle Ordovician, which eventually induced the united Dananhu–Harlik arc system (Du et al., 2021; Xiao et al., 2004; Zhang et al., 2018). Such model is favored here as it can fit most of the regional geological features (Du et al., 2021; Ma, 1999; Mao et al., 2022; Xiao et al., 2004; Zhang et al., 2017, 2018, 2020). Firstly, the oldest
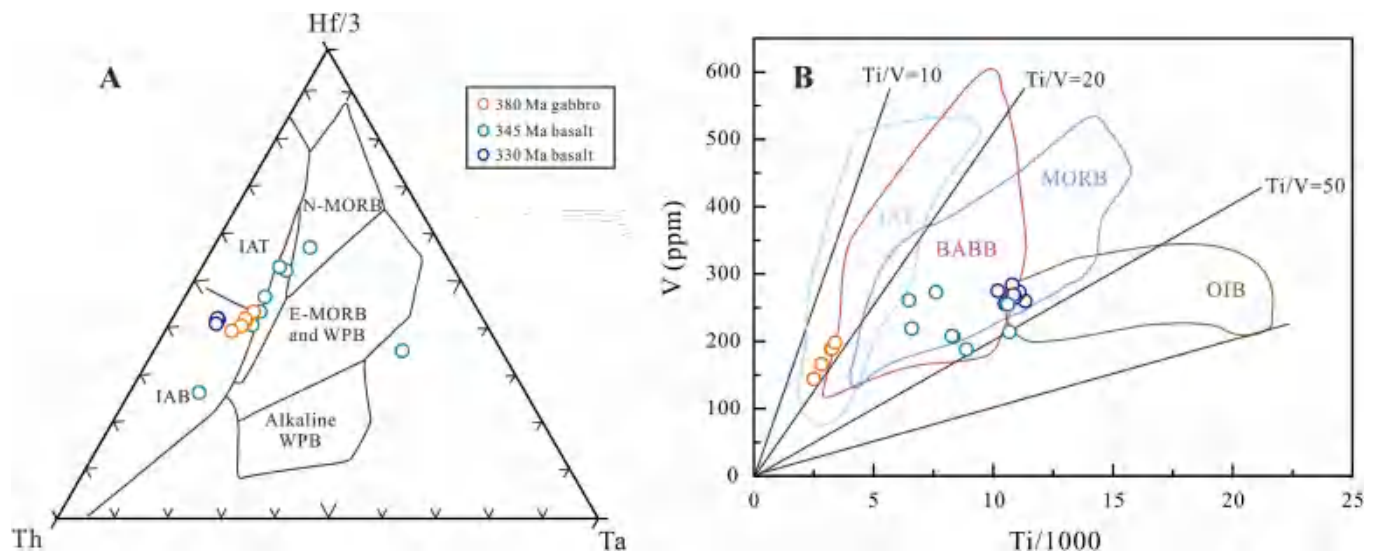

Fig. 10. (A) Plot of Hf/3–Th–Ta (after Wood, 1980). (B) Plot of V versus Ti/1000 (after Shervais, 1982). IAT, island arc tholeiitic basalt; IAB, island arc calc-alkaline basalt; WPB, within-plate basalt; BABB, back-arc basin basalt. The data for the 345 Ma and 330 Ma basalts in the Bogda back-arc basin are from Chen et al. (2013) and Zhang et al. (2017), respectively.

(Middle to Late Ordovician) arc-related magmatic rocks have been both identified in the Harlik belt and the Dananhu belt, and the arc magmatism show a younging trend accompanied by decreasing magmatic volumes from north to south, which can be comparable to the volcanic front to the back-arc side in the Japan arc system (Du et al., 2018, 2021; Kogiso et al., 2009; Mao et al., 2022). Secondly, it is found that the consistence of the earliest Ordovician to Silurian sedimentary strata occurred both in the Harlik and Dananhu arcs (Du et al., 2019; Ma, 1999). Finally, lithologically, the Ordovician to Silurian strata in the Harlik area are dominated by passive margin-like clastic sediments (Zhang et al., 2018, 2020), while those in the Dananhu area are composed mainly of active margin-like arc volcanic and intrusive rocks (Mao et al., 2022; Xiao et al., 2004).

Back-arc spreading has been associated with subduction since the early days of plate tectonics, and according to the absence or existence of actively opening back-arc basins, subduction zones are generally classified into two types, the Andean type and the Mariana type (Collins, 2002; Liu et al., 2022; Magni, 2019; Sdrolias and Müller, 2006). Thus, the formation of back-arc basins is crucial for understanding the development of accretionary orogenies (Collins, 2002; Liu et al., 2022; Magni, 2019; Sdrolias and Müller, 2006). For the Eastern Tianshan, there are still doubts about the initial stretching time of the back-arc basin and its relation to this Paleozoic accretionary orogen (Du et al., 2021; Xiao et al., 2004; Zhang et al., 2018). Based on studies of the earliest (Early Carboniferous) stratum in the intervening Bogda mountain between the Dananhu and Harlik belts, which is dominated by littoral-neritic facies clastic sediments and biolimestone with fossils assemblages, reflecting a marine environment (Shu et al., 2011). Combined with reported Early Carboniferous (ca. 345 Ma and 330 Ma) bimodal volcanic suites in the Bogda belt, which show both intraplate- and arc-like magmatic affinities (Chen et al., 2013; Zhang et al., 2017). The above evidence assumed that the Bogda back-arc basin was formed during Early Carboniferous. Alternatively, the opening of the Bogda back-arc basin seems to have occurred before Early Carboniferous as a response to the distinct distribution range of the magmatic rocks, as well as their geochemical and isotopic compositions before and after Late Devonian (ca. 380 Ma) in the Eastern Tianshan (e.g., Du et al., 2021; Zhang et al., 2018). However, no solid evidence has previously been observed for the Late Devonian back-arc setting, casting a shadow on this model.

The Late Devonian (ca. 380 Ma and 361 Ma) high-Al mafc and A-type felsic magmatism and inferred mantle and crust sources in this study help to refine the subduction process and further constrain the initial transition from subduction to back-arc extension. As mentioned above, the Kezier high-Al gabbros display high Al_2O_3 contents and positive Eu and Sr anomalies (Fig. 5C, D), which could be attributed to hydrous at a relatively shallow depth conditions (Xie et al., 2016; Xu et al., 2020). Moreover, the Kezier gabbros have relatively high Th but low Ta contents and plot in the field of calc-alkaline arc basalts on a Hf/3–Th–Ta discrimination diagram (Fig. 10A; Wood, 1980). They have relatively low Ti contents and Ti/V ratios, identical to the compositions of basalts formed in a back-arc setting, in which their compositions are controlled by pressure-release partial melting (Fig. 10B; Shervais, 1982; Grevemeyer et al., 2021). Hence, the initial back-arc basin-related magmatism is probably formed in the Dananhu belt instead of Bogda belt, similar to the Okinawa Trough behind the Ryukyu arc–trench system and the Lau basin with the Valu Fa ridge (Martinez and Taylor, 2002; Shinjo and Kato, 2000). In this scene, melts delivered under the volcanic arc are overturned and reintroduced beneath the back-arc spreading ridge by subduction-induced corner flow (Grevemeyer et al., 2021; Martinez and Taylor, 2002). This was coincident with the Early Carboniferous high-Al basalts from the Bogda area have more primitive basaltic component than the Late Devonian gabbros in the Dananhu belt (Figs. 5, 6, and 10; Chen et al., 2013; Zhang et al., 2017). Further, due to the arc splits and decompression melting of the asthenosphere in the back-arc region, the thinned crust is exceptionally hot, and crustal high-temperature melting
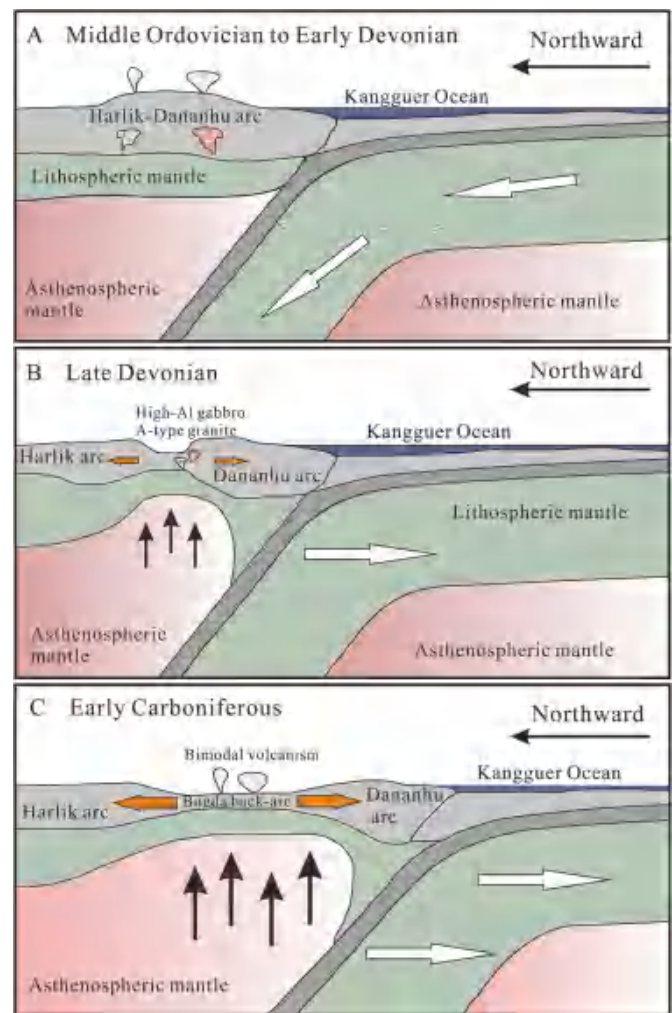
Fig. 11. Schematic cartoons illustrating tectonic evolution of the Eastern Tianshan during the Paleozoic. (A) Northward subduction of the Kangguer oceanic slab led to the formation of the Harlik-Dananhu arc during the Middle Ordovician to Early Devonian. (B) At Late Devonian, Kangguer oceanic plate southward retreat induces initial back-arc rifting occur on the Dananhu side. (C) The Kangguer oceanic slab persistently southward rollback gave rise to regional extension and forced the back-arc spreading centre move to the Bogda area during the Early Carboniferous.

is inevitable (Collins, 2002). Thus, the 380–361 Ma A-type magmatism in the Dananhu belt corresponds to this crustal high-temperature melting event. Moreover, the coeval magmatism was active in the Kezier area of the Dananhu belt, such as the 380–390 Ma adakitic granitic rocks (Mao et al., 2022) and ca. 370 Ma mantle-derived basalts and dacites (Zhang et al., 2018). Given that these Late Devonian specific magmatism were identifed in the Eastern Tianshan, tectonic transition from arc to back-arc basin was likely initiated during this period.

Additionally, the formation of back-arc basins can be driven mainly by the rollback of the subducting slab or by the absolute motion of the overriding plate (Collins, 2002; Magni, 2019; Sdrolias and Müller, 2006). It is worth noting that the Late Devonian back-arc extension was nearly coeval with the onset of the earliest arc magmatic records southward rejuvenating from the Dananhu arc, through Kangguer suture zone (e.g., ca. 360 Ma porphyritic granite near the Kangguer fault), to the Yamansu area (e.g., the Yamansu Formation which started at 348 Ma) (Du et al., 2018, 2021; Luo et al., 2012; Zhang et al., 2018). On the other hand, the crustal high-temperature melting responsible for the A-type magmatism northward rejuvenating (ca. 380–361 Ma in the Dananhu belt, to ca. 345–330 Ma in the Bogda belt), in accordance with

the zircon saturation temperature for these A-type magmatism from ca. 380 Ma to ca. 345 Ma showing rising trend (Fig. 9B). Accordingly, it is reasonable to infer that the southward rollback of the Kangguer oceanic slab produced the retreating arc magmatism, triggered the overriding plate extension, and was most likely responsible for the prolonged Dananhu–Bogda–Harlik arc–back-arc system (Fig. 11). Such a scenario would squeeze the mantle wedge asthenosphere out and force the melt zone toward back-arc side, corresponding to the magmatic migration from the Dananhu arc to the Bogda side (Chen et al., 2013; Zhang et al., 2017). An analogous driving mechanism of back-arc basin formation has also used to explain the concentration of back-arc basins in the western Pacific margins (Grevemeyer et al., 2021; Magni, 2019; Sdrolias and Müller, 2006). Collectively, the Kangguer oceanic lithosphere rollback forced the initial arc rifting occur on the Dananhu fore-arc side since the Late Devonian (Fig. 11B), and then the back-arc spreading centre move to the Bogda area (Fig. 11C), which can provides an internally consistent explanation for all of these geological events.

5. Conclusions

1. The Kezier mafic–felsic complex and Tuwu granitic pluton were emplaced during the Late Devonian.
2. The gabbros show characteristics of high-Al basalts and were formed by hydrous pressure-release partial melting.
3. The granites belong to A-type granites and were derived from high-temperature and low-pressure melting of juvenile crust.
4. The Eastern Tianshan arc–back-arc system was extension during the Late Devonian formed by southward rollback of the Kangguer oceanic slab.

Declaration of Competing Interest

The authors declare that they have no known competing financial interests or personal relationships that could have appeared to influence the work reported in this paper.

Acknowledgements

Appendix A. Supplementary data

Supplementary data to this article can be found online at https://doi.org/10.1016/j.lithos.2023.107283.

References

Allegre, C.J., Minster, J.F., 1978. Quantitative models of trace element behavior in magmatic processe. Earth Planet. Sci. Lett. 38, 1–25.

Beard, J.S., Lofgren, G.E., 1992. An experiment-based model for the petrogenesis of high alumina basalts. Science 258, 112–115.

Belousova, E.A., Griffin, W.L., O'Reilly, S.Y., Fisher, N.I., 2002. Igneous zircon: trace element composition as an indicator of source rock type. Contrib. Mineral. Petrol. 143, 602–622.

Bonin, B., 2007. A-type granites and related rocks: evolution of a concept, problems and prospects. Lithos 97, 1–29.

Cawood, P.A., Kröner, A., Collins, W.J., Kusky, T.M., Mooney, W.D., Windley, B.F., 2009. Accretionary orogens through Earth history. Geol. Soc. Lond., Spec. Publ. 318, 1–36.

Charvet, J., Shu, L.S., Laurent-Charvet, S., 2007. Paleozoic structural and geodynamic evolution of eastern Tianshan (NW China): welding of the Tarim and Junggar plates. Episodes 30, 162–186.

Chen, X.J., Shu, L.S., Santosh, M., Zhao, X.X., 2013. Island arc-type bimodal magmatism in the Eastern Tianshan Belt, Northwest China: geochemistry, zircon U-Pb geochronology and implications for the Paleozoic crustal evolution in Central Asia. Lithos 168–169, 48–66.

Chen, Z.Y., Xiao, W.J., Windley, B.F., Schulmann, K., Mao, Q.G., Zhang, Z.Y., Zhang, J.E., Deng, C., Song, S.H., 2019. Composition, provenance, and tectonic setting of the Southern Kangurtag accretionary complex in the Eastern Tianshan, NW China: implications for the late paleozoic evolution of the North Tianshan Ocean. Tectonics 38, 2779–2802.

Collins, W.J., 2002. Hot orogens, tectonic switching, and creation of continental crust. Geology 30, 535–538.

Crawford, A.J., Falloon, T.J., Eggins, S., 1987. The origin of island arc high alumina basalts. Contrib. Mineral. Petrol. 97, 417–430.

Deng, X.H., Wang, J.B., Pirajno, F., Wang, Y.W., Li, Y.C., Li, C., 2016. Re–Os dating of chalcopyrite from selected mineral deposits in the Kalatag district in the eastern Tianshan Orogen, China. Ore Geol. Rev. 77, 72–81.

Du, L., Long, X.P., Yuan, C., Zhang, Y.Y., Huang, Z.Y., Wang, X.Y., Yang, Y.H., 2018. Mantle contribution and tectonic transition in the Aqishan Belt, Eastern Tianshan, NW China: insights from geochronology and geochemistry of early carboniferous to early permian felsic intrusions. Lithos 304–307, 230–244.

Du, L., Yuan, C., Li, X.P., Zhang, Y.Y., Huang, Z.Y., Long, X.P., 2019. Petrogenesis and geodynamic implications of the carboniferous granitoids in the Dananhu belt, Eastern Tianshan orogenic belt. J. Earth Sci. 30, 1243–1252.

Du, L., Zhu, H.L., Yuan, C., Zhang, Y.Y., Huang, Z.Y., Li, X.-P., Long, X.P., 2021. Paleozoic crustal evolution and tectonic switching in the Northeastern Tianshan: insights from zircon Hf isotopes of granitoids. J. Geol. Soc. Lond. 178 jgs2020–035.

Eby, G.N., 1990. The A-type granitoids: a review of their occurrence and chemical characteristics and speculations on their petrogenesis. Lithos 26, 115–134.

Eby, G.N., 1992. Chemical subdivision of the A-type granitoids: petrogenetic and tectonic implications. Geology 20, 641–644.

Ferrari, L., 2004. Slab detachment control on mafc volcanic pulse and mantle heterogeneity in Central Mexico. Geology 32, 77–80.

Frey, F.A., Green, D.H., Roy, S.D., 1978. Integrated models of basalt petrogenesis: a study of quartz tholeiites to olivine melilitites from South Eastern Australia utilizing geochemicaland experimental petrological data. J. Petrol. 19, 463–513.

Gao, J., Qian, Q., Long, L.L., Zhang, X., Li, J.L., Su, W., 2009. Accretionary orogenic process of Western Tianshan, China. Geolog. Bullet. China 28, 1804–1816 (in Chinese with English abstract).

Gao, J.F., Zhou, M.F., Qi, L., Chen, W.T., Huang, X.W., 2015. Chalcophile elemental compositions and origin of the Tuwu porphyry Cu deposit, NW China. Ore Geol. Rev. 66, 403–421.

Green, N.L., 2006. Influence of slab thermal structure on basalt source regions and melting conditions: REE and HFSE constraints form the Garibaldi volcanic belt, northern Cascadia subduction system. Lithos 87, 23–49.

Grevemeyer, I., Kodaira, S., Fujie, G., Takahashi, N., 2021. Structure of oceanic crust in back-arc basins modulated by mantle source heterogeneity. Geology 49, 468–472.

Han, Y.G., Zhao, G.C., 2018. Final amalgamation of the Tianshan and Junggar orogenic collage in the southwestern Central Asian Orogenic Belt: constraints on the closure of the Paleo-Asian Ocean. Earth Sci. Rev. 186, 129–152.

Harris, R.A., 2004. Geodynamic patterns of ophiolites and marginal basins of the Indonesian and New guinea regions. In: Dilek, Y., Robinson, P.T. (Eds.), Ophiolites in Earth History, Geological Society, London, Special Publication, vol. 218, pp. 481–505.

Hofmann, A.W., 1997. Mantle geochemistry: the message from oceanic volcanism. Nature 385, 219–229.

Huang, Z.Y., Long, X.P., Wang, X.C., Zhang, Y.Y., Du, L., Yuan, C., Xiao, W.J., 2017. Precambrian evolution of the Chinese Central Tianshan Block: constraints on its tectonic affinity to the Tarim Craton and responses to supercontinental cycles. Precambrian Res. 295, 24–37.

Jahn, B.M., Wu, F.Y., Chen, B., 2000. Granitoids of the Central Asian orogenic belt and continental growth in the phanerozoic. In: Transactions of the Royal Society Edinburgh: Earth Sciences, 91, pp. 181–193.

Johnson, A.D., 1986. Anhydrous P–T phase relations of near-primary high-alumina basalt from the South Sandwich Islands. Contrib. Mineral. Petrol. 92, 368–382.

Johnson, K.T.M., 1994. Experimental cpx/ and garnet/melt partitioning of REE and other trace elements at high pressures; petrogenetic implications. Min. Mag. 58, 454–455.

Kemp, A.I.S., Wormald, R.J., Whitehouse, M.J., Price, R.C., 2005. Hf isotopes in zircon reveal contrasting sources and crystallization histories for alkaline to peralkaline granites of Temora, southeastern Australia. Geology 33, 797–800.

Kogiso, T., Omori, S., Maruyama, S., 2009. Magma genesis beneath Northeast Japan arc: a new perspective on subduction zone magmatism. Gondwana Res. 16, 446–457.

Kuno, H., 1960. High-alumina basalt. J. Petrol. 1, 121–145.

Li, W.Q., Ma, H.D., Wang, R., Wang, H., Xia, B., 2008. SHRIMP dating and Nd-Sr isotopic tracing of Kanggurtage ophiolite in eastern Tianshan, Xinjiang. Acta Petrol. Sin. 4, 773–780 (in Chinese with English abstract).

Liu, X.Y., Zhang, Q., Zhang, C.L., 2022. Identification of the original tectonic setting for oceanic andesite using discrimination diagrams: an approach based on global geochemical data synthesis. J. Earth Sci. 33, 696–705.

Long, X.P., Wu, B., Sun, M., Yuan, C., Xiao, W.J., Zuo, R., 2020. Geochronology and geochemistry of late Carboniferous dykes in the Aqishane-Yamansu belt, eastern Tianshan: evidence for a post-collisional slab breakoff. Geosci. Front. 11, 347–362.

Luo, T., Liao, Q.A., Chen, J.P., Zhang, X.H., Guo, D.B., Hu, Z.C., 2012. LA-ICP-MS zircon U–Pb dating of the volcanic rocks from Yamansu Formation in the Eastern Tianshan, and its geological significance. Earth Sci. J. China Univ. Geosci. 6, 1338–1352 (in Chinese with English abstract).

Ma, J.C., 1999. Study on the Huangcaopo Group in the eastern Junggar. J. Mineral. Petrol. 19, 52–55 (in Chinese with English abstract).

Ma, X.X., Shu, L.S., Meert, J.G., 2015. Early Permian slab breakoff in the Chinese Tianshan belt inferred from the post-collisional granitoids. Gondwana Res. 27, 228–243.

Magni, V., 2019. The effects of back-arc spreading on arc magmatism. Earth Planet. Sci. Lett. 519, 141–151.

Mao, Q.G., Xiao, W.J., Fang, T.H., Windley, B.F., Sun, M., Ao, S.J., Zhang, J.E., Huang, X. K., 2014. Geochronology, geochemistry and petrogenesis of early Permian alkaline magmatism in the Eastern Tianshan: implications for tectonics of the Southern Altaids. Lithos 190–191, 37–51.

Mao, Q.G., Ao, S.J., Windley, B.F., Song, D.F., Sang, M., Tan, Z., Wang, H., Li, R., Xiao, W.J., 2022. Late paleozoic southward migration of the dananhu arc in the Eastern Tianshan (NW China). Earth Space Sci. 9 e2021EA002027.

Márquez, A., Oyarzun, R., Doblas, M., Verma, S.P., 1999. Alkalic (OIB-type) and calcalkalic volcanism in the Mexican volcanic belt: a case of plume-related magmatism and propagating rifting at an active margin? Geology 27, 51–54.

Martinez, F., Taylor, B., 2002. Mantle wedge control on back-arc crustal accretion. Nature 416, 417–420.

Mckenzie, D.A.N., O'nions, R.K., 1991. Partial melt distributions from inversion of rare earth element concentrations. J. Petrol. 32, 1021–1091.

Patiño Douce, A.E., Beard, J.S., 1995. Dehydration–melting of biotite and quartz amphibolite from 3 to 15 kb. J. Petrol. 36, 707–738.

Pearce, J.A., 2008. Geochemical fingerprinting of oceanic basalts with applications to ophiolite classification and the search for Archean oceanic crust. Lithos 100, 14–48.

Pearce, J.A., Stern, J.R., Bloomer, S.H., Fryer, P., 2005. Geochemical mapping of the Mariana arc-basin system: implications for the nature and distribution of subduction components. Geochem. Geophys. Geosyst. 6, 1–27.

Qin, K.Z., Su, B.X., Sakyi, P.A., Tang, D.M., Li, X.H., Sun, H., Xiao, Q.H., Liu, P.P., 2011. SIMS zircon U–Pb geochronology and Sr–Nd isotopes of Ni-Cu-bearing mafic–ultramafic intrusions in Eastern Tianshan and Beishan in correlation with flood basalts in Tarim basin (NW China): constraints on a ca. 280 Ma mantle plume. Am. J. Sci. 311, 237–260.

Rudnick, R.L., Fountain, D.M., 1995. Nature and composition of the continental crust: a lower crustal perspective. Rev. Geophys. 33, 267–309.

Rudnick, R.L., Gao, S., 2003. Composition of the Continental Crust, 3. Elsevier-Pergamon, Oxford, pp. 1–64.

Sdrolias, M., Müller, R.D., 2006. Controls on back-arc formation. Geochem. Geophys. Geosyst. 7, Q04016.

Shervais, J.W., 1982. Ti–V plots and the petrogenesis of modern and ophiolitic lavas. Earth Planet. Sci. Lett. 59, 101–118.

Shinjo, R., Kato, Y., 2000. Geochemical constraints on the origin of bimodal magmatism at the Okinawa Trough, an incipient back-arc basin. Lithos 54, 117–137.

Shu, L.S., Wang, B., Zhu, W.B., Guo, Z.J., Charvet, J., Zhang, Y., 2011. Timing of initiation of extension in the Tianshan, based on structural, geochemical and geochronological analyses of bimodal volcanism and olistostrome in the Bogda Shan (NW China). Int. J. Earth Sci. 100, 1647–1663.

Sisson, T.W., Grove, T.L., 1993. Temperatures and H$_2$O contents of low-MgO high-alumina basalts. Contrib. Mineral. Petrol. 113, 167–184.

Sun, S.S., McDonough, W.F., 1989. Chemical and isotopic systematics of oceanic basalts: implications for mantle composition and processes. Geol. Soc. Lond., Spec. Publ. 42, 313–345.

Tang, G.J., Chung, S.L., Wang, Q., Wyman, D.A., Dan, W., Chen, H.Y., Zhao, Z.H., 2014. Petrogenesis of a late Carboniferous mafic dike–granitoid association in the western Tianshan: response to the geodynamics of oceanic subduction. Lithos 202–203, 85–89.

Tao, Z.L., Yin, J.Y., Chen, W., Chen, Y.L., Sun, J.B., Xu, Z.H., 2022. Zircon U–Pb ages and tectonic implications of late Paleozoic volcanic rocks in the Western Tianshan, North Xinjiang, China. J. Earth Sci. 33, 736–752.

Wagner, T.P., Donnelly-Nolan, J.M., Grove, T.L., 1995. Evidence of hydrous differentiation and crystal accumulation in the low-MgO, highAl$_2$O$_3$ Lake basalt from medicine Lake volcano, California. Contrib. Mineral. Petrol. 121, 201–216.

Wang, B., Cluzel, D., Jahn, B.M., Shu, L.S., Chen, Y., Zhai, Y.Z., Branquet, Y., Barbanson, L., Sizaret, S., 2014. Late Paleozoic pre- and syn-kinematic plutons of the Kangguer-Huangshan Shear zone: inference on the tectonic evolution of the Eastern Chinese North Tianshan. Am. J. Sci. 314, 43–79.

Wang, Y.H., Zhang, F.F., Xue, C.J., Liu, J.J., Zhang, Z.C., Sun, M., 2021. Geology and Genesis of the Tuwu Porphyry Cu Deposit, Xinjiang, Northwest China. Econ. Geol. 116 (2), 471–500.

Wang, G.C., Zhang, M., Zhang, X.H., Kang, L., Liao, Q.A., Guo, R.L., Wang, W., 2022. Re-understanding on the tectonic implication and evolutional model of the "North Tianshan Ocean" from the eastern Tianshan area, Xinjiang, NW China. Acta Geol. Sin. 96, 3494–3513 (in Chinese with English abstract).

Watson, E.B., Harrison, T.M., 1983. Zircon saturation revisited: temperature and composition effects in a variety of crustal magma types. Earth Planet. Sci. Lett. 64, 295–304.

Whalen, J.B., Currie, K.L., Chappell, B.W., 1987. A-type granites: geochemical characteristics, discrimination and petrogenesis. Contrib. Mineral. Petrol. 95, 407–419.

Wilhem, C., Windley, B.F., Stampfli, G.M., 2012. The Altaids of Central Asia: a tectonic and evolutionary innovative review. Earth Sci. Rev. 113, 303–341.

Windley, B.F., Allen, M.B., Zhang, C., Zhao, Z.Y., Wang, G.R., 1990. Paleozoic accretion and Cenozoic redeformation of the Chinese Tien Shan Range, Central Asia. Geology 18, 128.

Windley, B.F., Alexeiev, D., Xiao, W., Kröner, A., Badarch, G., 2007. Tectonic models for accretion of the Central Asian Orogenic Belt. J. Geol. Soc. Lond. 164, 31–47.

Wood, D.A., 1980. The application of a Th–Hf–Ta diagram to problems of tectonomagmatic classification and to establishing the nature of crustal contamination of basaltic lavas of the British Tertiary Volcanic Province. Earth Planet. Sci. Lett. 50, 11–30.

Woodhead, J.D., Hergt, J.M., Davidson, J.P., Eggins, S.M., 2001. Hafnium isotope evidence for 'conservative' element mobility during subduction zone processes. Earth Planet. Sci. Lett. 192, 331–346.

Xiao, W.J., Zhang, L.C., Qin, K.Z., Sun, S., Li, J.L., 2004. Paleozoic accretionary and collisional tectonics of the Eastern Tianshan (China): implications for the continental growth of Central Asia. Am. J. Sci. 304, 370–395.

Xie, W., Xu, Y.G., Chen, Y.B., Luo, Z.Y., Hong, L.B., Ma, L., Liu, H.Q., 2016. High-alumina basalts from the Bogda Mountains suggest an arc setting for Chinese Northern Tianshan during the late carboniferous. Lithos 256–257, 165–181.

Xiong, X.L., Adam, J., Green, T.H., 2005. Rutile stability and rutile/melt HFSE partitioning during partial melting of hydrous basalt: implications for TTG genesis. Chem. Geol. 218, 339–359.

Xu, Y.G., Wang, Q., Tang, G.J., Wang, J., Li, H.Y., Zhou, J.S., Li, Q.W., Qi, Y., Liu, P.P., Ma, L., Fan, J.J., 2020. The origin of arc basalts: New advances and remaining questions. Sci. China Earth Sci. 63, 1969–1991.

Yuan, C., Sun, M., Wilde, S., Xiao, W.J., Xu, Y.G., Long, X.P., Zhao, G.C., 2010. Post-collisional plutons in the Balikun area, East Chinese Tianshan: evolving magmatism in response to extension and slab break-off. Lithos 119, 269–288.

Zhang, X.R., Zhao, G.C., Sun, M., Eizenhöfer, P.R., Han, Y.G., Hou, W.Z., Liu, D.X., Wang, B., Liu, Q., Xu, B., 2016. Tectonic evolution from subduction to arc-continent collision of the Junggar Ocean: constraints from U-Pb dating and Hf isotopes of detrital zircons from the North Tianshan Belt, NW China. Geol. Soc. Am. Bull. 128, 644–660.

Zhang, Y.Y., Yuan, C., Long, X.P., Sun, M., Huang, Z.Y., Du, L., Wang, X.Y., 2017. Carboniferous bimodal volcanic rocks in the Eastern Tianshan, NW China: evidence for arc rifting. Gondwana Res. 43, 92–106.

Zhang, Y.Y., Sun, M., Yuan, C., Long, X.P., Jiang, Y.D., Li, P.F., Huang, Z.Y., Du, L., 2018. Alternating trench advance and retreat: insights from Paleozoic magmatism in the Eastern Tianshan, Central Asian Orogenic Belt. Tectonics 37, 2142–2164.

Zhang, Y.Y., Yuan, C., Sun, M., Long, X.P., Huang, Z.Y., Jiang, Y.D., Li, P.F., Du, L., 2020. Two late Carboniferous belts of Nb-enriched mafic magmatism in the Eastern Tianshan: heterogeneous mantle sources and geodynamic implications. Geol. Soc. Am. Bull. 132, 1863–1880.

Zhang, F.F., Wang, Y.H., Liu, J.J., Xue, C.J., Wang, J.P., Zhang, W., Li, Y.Y., 2022a. Paleozoic magmatism and mineralization potential of the Sanchakou Copper Deposit, Eastern Tianshan, Northwest China: insights from geochronology, mineral chemistry, and isotopes. Econ. Geol. 117 (1), 165–194.

Zhang, X.N., Zeng, Q.D., Nie, F.J., 2022b. Geochemical variations of the Late Paleozoic granitoids from the Baolidao arc-accretion belt in southeastern segment of Central Asia Orogenic Belt:implications for tectonic transition from Early Carboniferous to Early Permian. J. Earth Sci. 33, 719–735.

Zhao, J., Zhou, M., 2009. Secular evolution of the neoproterozoic lithospheric mantle underneath the northern margin of the Yangtze block, South China. Lithos 107, 152–168.